CrystEngComm

PAPER



Cite this: *CrystEngComm*, 2018, **20**, 5801

# $ZnO–TiO_2$ composites and ternary $ZnTiO_3$ electrospun nanofibers: the influence of annealing on the photocatalytic response and reusable functionality†

Kugalur Shanmugam Ranjith* and Tamer Uyar*

The developments in environmental remediation based on the advanced oxidation processes of catalyst surfaces still endure the burden of the effective recombination of photoinduced charge carriers. The construction of defect band levels with heterostructural phases of catalytic nanostructures is a tenable strategy for separating photogenerated charge carriers and for minimizing carrier recombination. Herein, we explain an effective carrier separation rate with extended light absorption using electrospun ZnTi-based semiconducting nanofibers, which feature as composites and ternary form for their structural geometry. We explain the effective surface functionality with the design of the $ZnO–TiO_2$ composite and $ZnTiO_3$ as a function of the annealing temperature on electrospun fibers, and their commendable visible catalytic properties with the presence of defect states for degrading organic pollutants. The constructed $ZnTiO_3$ in the form of nanofibers induced a narrow band gap of 3.01 eV as compared with its individual counterparts (ZnO (3.27 eV) and $TiO_2$ (3.17 eV)). However, the composite functionality has an advantage in inducing discrete defect levels with the carbon impurities for favorable extended visible absorption with a similar morphological nature. Under visible irradiation, the ternary form of the nanofibers exhibited a photocatalytic degradation performance of around 72.45% and the composite fibers exhibited one of around 95.82% in 125 min due to the scrutinized function of the defect states that maximize the interfacial charge transfer between ZnO–C–$TiO_2$ and delay the carrier recombination rate. The reliable mechanism behind the charge transfer of the photogenerated carriers was supported by trapping experiments of two different geometrical nanostructures on degrading organic pollutants. The interesting results obtained from the stability and reusability studies were that the $ZnO–TiO_2$ composite nanofibers have a notably surface photocorrosive nature after catalytic reaction but the ternary $ZnTiO_3$ form of the nanofibers has a stable surface stability with stable reusable catalytic functionality for up to 20 consecutive cycles. Constructing the nanostructures with tunable surface structural natures anticipates the broad possibilities in the photocatalytic realm for achieving improved visible catalytic responses with stable and reusable functionality over their single counterparts.

Received 3rd June 2018,
Accepted 16th August 2018

DOI: 10.1039/c8ce00920a

rsc.li/crystengcomm

## Introduction

Currently, the issues of the environmental hazards of industrial organic wastes and harmful water pollutants are being extensively investigated using semiconductor photocatalysts for improved environmental sustainability. Among the surfeit of semiconductor catalysts, $TiO_2$ and ZnO are the promising ones that are considered as effective catalysts for eliminating organic pollutants with incomparable efficiency with tunable surfaces and structural functionality.[1,2] To make it worth commercializing a semiconductor photocatalyst, it has to exhibit superior photocatalytic activity with a broad light responsive nature, especially under visible irradiation. However, the known effective catalysts such as ZnO and $TiO_2$ have limits under UV irradiation because of their wide band functionality that can utilize only 3–5% of the solar spectrum.[3–5] Mostly, the single counterparts of semiconductor nanostructures assist the effective carrier recombination of photoinduced electron hole pairs and considerably curtail their quantum efficiency.[6,7] To migrate away from these issues, these wide band gap semiconductors have to reinforce their visible

*Institute of Materials Science & Nanotechnology and UNAM–National Nanotechnology Research Center, Bilkent University, Ankara, 06800, Turkey. E-mail: tamer@unam.bilkent.edu.tr, ranjuphy@gmail.com*

† Electronic supplementary information (ESI) available: Synthesis procedures for ZnO and $TiO_2$ NFs, XRD of different temperature annealed NF samples and BET results, 4-CP and MB degradation under visible irradiation, ROS quantification experiments, dye degradation spectra with respect to time, optical and XRD spectra after catalytic recycling measurements of $ZnO–TiO_2$ and $ZnTiO_3$ NF. See DOI: 10.1039/c8ce00920a

activity with an effective carrier separation rate. The construction of the one dimensional (1D) forms of nanostructures, such as nanorods, nanotubes and nanofibers (NFs), has provided evidence for an improved light harvesting efficiency and has enhanced the collection of photoinduced charge carriers.[8–10] Additionally, intergrading the defect states and designing the heterostructural nature is being established as a thriving approach towards enhancing catalytic efficiency and improving the carrier separation rate willingly under visible irradiation.[11–13] Narrow band gap metal-chalcogenide-based shell functionality was preferably decorated over wide band gap semiconductors as sensitizers to extend their broad spectral adsorption with high extinction coefficients under lower photon energy.[14–16] However, the initiated environmental concerns are a serious issue for the catalyst, and will not allow for the clean environmental demand. In this view, integrating the two environmentally safer wide band gap semiconductors ($TiO_2$ and ZnO) with their unique structural features in ternary form with tunable defect and impurity states offers a potential platform, with fiber morphology gained through the electrospinning process.[17] The electrospinning process offers a synthesis protocol for a vast set of semiconducting nanostructures with different atomic ratios and distinct heterostructures in a 1D fiber morphology to give tunable functional properties.[18–20] The tunable structural nature, along with the function of the annealing temperature, realizes the construction of a composite in the ternary phase, with a significant visible catalytic response. Offering different band offsets with the 1D NF morphology that effectively separate the photogenerated charge carriers leads to a delay in the carrier recombination rate.[3] Compositing $ZnTiO_3$ in the form of nanograins in a fiber morphology with a polymeric chain will induce carbon impurity phases after decomposing the polymeric groups through an annealing process, which promotes the carrier interaction between the metal oxide nanograins. Even though the carbon impurities are not the main factor of the catalytic surface, they lead to participation in the carrier mobility and to surface protective features, and they improve the catalytic activity. The effect of the annealing temperature will influence the structural nature and the tunable surface impurities. It will control the ionic mobility with a controlled certain ternary form at the surface depending on the ionic ratio. The participation of dual metal ionic functionality in different forms with the oxide phase with similar morphological aspects would play a role in influencing the separation rate of photoinduced charge carriers depending on the ionic ratio and the nature of the surface crystal structure. The anticipation of surface functionality from the composite to the ternary phase leads to the proper band offset with the 1D morphology with the function of the annealing temperature. Using understanding from the construction of composites to ternary-phased 1D NFs, we design a layout for ZnO–$TiO_2$ composites and $ZnTiO_3$ electrospun NFs with different band structures as a function of the annealing temperature with the possibility of defect states. Both forms of the heterostructure induced commendable visible photocatalytic responses towards the degradation of organic pollutants with an effective production of reactive oxygen species (ROS). However, the follow-on point over the effective visible response, catalytic stability and reusable performance is that the structural features of the composites and ternary NFs have their own advantages that highlight them as better catalysts. The presence of carbon-based impurities and the structural nature of the catalyst were propitious for an effective carrier mobility with an improved visible response. The scrutinized factors favor the effective carrier separation in the heterostructure, but the composite form with the favorable defect states facilities the carrier mobility and improves the visible photoresponsivity. Furthermore, this work initiates an understanding of the structural stability and reusable performance of the catalytic NFs with the function of different surface crystalline natures and speculates about the construction of feasible and durable photocatalysts that are environmentally sustainable. We predict that our investigation will reveal the potential advantages of the surface structural design for the construction of visible responsive heterostructural NFs with tunable structural merits for improving environmentally sustainable photocatalysts.

## Experimental section

### Materials

Polyvinylpyrrolidone (PVP, Mw = 1 300 000, Sigma-Aldrich), zinc acetate ($Zn(OAc)_2$, Sigma-Aldrich), titanium(IV) butoxide ($Ti(OBu)_4$, Sigma-Aldrich), ethanol ($C_2H_5OH$, Sigma-Aldrich), acetic acid ($CH_3COOH$, Sigma-Aldrich), methylene blue (MB, Sigma-Aldrich), 4-cholorophenol (99%, 4-CP, Alfa Aesar), nitroblue tetrazolium chloride (NBT, Alfa Aesar), chlorobenzoic acid (*p*-CBA, Sigma-Aldrich), *p*-benzoquinone (98%, BQ, Alfa Aesar), triethonalamine, (99%, TEOA, Sigma-Aldrich), silver nitrate ($AgNO_3$, Sigma-Aldrich), isopropyl alcohol (99.5% IPA, Sigma-Aldrich), and Degussa P25 were procured, and were used as received without any further purification.

### The electrospinning of $Zn(OAc)_2$–$Ti(OBu)_4$-PVP NFs

The synthesis of $Zn(OAc)_2$–$Ti(OBu)_4$-PVP NFs was accomplished using the electrospinning process. To prepare the electrospinning solution, 1 g of PVP was dissolved in 5 mL of ethanol with stirring. 1 mL of $Ti(OBu)_4$ and 4% (w/v) $Zn(OAc)_2$ were used as the Ti and Zn precursors and these were stirred for 20 minutes in 2 mL of ethanol and 0.6 mL of acetic acid; this solution was then added to the polymer solution. The resulting solution was stirred overnight and was then loaded into a 3 mL plastic syringe with a needle diameter of 0.4 mm. The syringe was placed horizontally on a syringe pump (KD scientific, KDS101) and given a flowrate of 0.5 mL $h^{-1}$. A grounded metal collector that was covered with aluminium foil was placed at a distance of 15 cm from the needle tip and an electric field (15.0 kV) was applied between the string and collector using a high voltage power supply (Spellman, SL series, USA). The electrospinning procedure was carried out at 22 °C and 19% relative humidity in a Plexiglas box.

 

The obtained $Zn(OAc)_2$–$Ti(OBu)_4$-PVP NFs were kept in the hood overnight to remove the residual solvent from the electrospun nanofibrous web.

### Synthesizing the ZnO–$TiO_2$ composite and the ternary $ZnTiO_3$ NFs

The annealing temperature influenced the different crystalline phases of the heterostructure during synthesis. Annealing the electrospun $Zn(OAc)_2$–$Ti(OBu)_4$-PVP NFs under a temperature of 500 °C for 3 hours initiated the synthesis of the ZnO–$TiO_2$ composite structure. At high temperatures (*i.e.* 500 °C), the organic parts of the electrospun $Zn(OAc)_2$–$Ti(OBu)_4$-PVP NFs started to decompose in the form of carbon impurities and were removed in the form of $CO_2$, while the acetic and butyl groups decomposed and the metal ions interacted with the oxide ions to transform into a mixed oxide phase of the ZnO–$TiO_2$ composite. In order to synthesis the ternary $ZnTiO_3$ NFs, the prepared ZnO–$TiO_2$ nanocomposite NFs were again calcined at 800 °C for 3 hours. When we directly annealed the $Zn(OAc)_2$–$Ti(OBu)_4$-PVP NF samples at 800 °C, it caused severe damage over the 1D morphology due to the faster decomposition of the polymer functionality. The resultant white-colored sponge-like product at higher temperatures is evidence of the complete removal of the carbon impurities. The temperature range 600–700 °C leads to the mixed phase formation of the ternary alloy phased with the ZnO and $TiO_2$ impurity phases, of which we weren't able to predict the structural functionality. Higher temperatures lead to the ionic mobility for the favorable synthesis of $ZnTiO_3$ NFs *via* the selective mobility of Zn ions to the catalytic surface. For the comparative investigations, $TiO_2$ and ZnO NFs were also synthesized through the electrospinning process, and these were compared with the functional heterostructural NFs.[13,21] Detailed experimental synthesis procedures of the ZnO and $TiO_2$ NFs are given in the supplementary information.

### Characterization

The structural purity and crystalline phases were analyzed through X-ray diffraction studies using a PANalytical X'Pert multipurpose X-ray diffractometer with Cu Kα radiation under a scan range ($2\theta$) from 10–70° with a scan rate of 0.02° $s^{-1}$. The morphology and surface structural features were explored using scanning electron microscopy (SEM, FEI-Quanta 200 FEG) equipped with an energy dispersive X-ray spectrometer (EDS). The detailed investigation on the structural finish and core–shell existence was carried out *via* transmission electron microscopy studies using an FEI-Tecnai G2 F30 electron microscope operating at an accelerating voltage of 200 kV. To support the difference in the existence of the composite and core–shell structure, these were furnished using the elemental mapping analysis on a scanning transmission electron microscope (STEM, Tecnai G2 F30, FEI). The light responsive nature was quantified *via* the UV-vis diffuse reflectance spectra obtained on a UV-vis spectrophotometer (Shimadzu UV-3600 spectrophotometer) and the band gaps of the nanostructures were calculated from the Kubelka–Munk relation. The surface chemical composition was analyzed using X-ray photoelectron spectroscopy (XPS, Thermo K-alpha-monochromated). The binding energies were referenced to the C 1s line at 284.8 eV from adventitious carbon. Photoluminescence (PL) measurements were performed using a time-resolved fluorescence spectrophotometer (FL- 1057 TCSPC) with an excitation wavelength at 350 nm. The specific surface areas of the samples were analyzed using the Brunauer–Emmet–Teller (BET) method carried out on a Quantachrome Instrument autosorb ($iQ_2$) analyzer after degassing the samples for 3 h at 200 °C.

### Photocatalytic performance

The photocatalytic activity of the catalytic NFs was investigated by investigating the degradation of MB as an organic pollutant. The evaluated catalytic performance of the $TiO_2$–ZnO composite, the ternary $ZnTiO_3$ NFs and their counterparts ($TiO_2$, ZnO) was investigated under UV (Ultra-Vitalux Ultraviolet high pressure lamp (300 W, Osram, sunlight simulation)) and visible (75 W xenon lamp accompanied with UV cut off filters ($\lambda < 400$)) irradiation. The catalytic activity was tested by dispersing 1 mg $mL^{-1}$ of the NF-based catalyst into quartz cuvettes containing the MB dye solution (15 ppm) and placing the cuvettes in the dark for 20 min to establish the adsorption/desorption equilibrium of the dye on the NF surface prior to irradiation. The working distance between the lamp and the catalyst was fixed as 15 cm and in the uniform interval time the absorption intensity of the dye solution was measured. Along with the series of different catalysts, the blank (without catalyst) was placed under photon irradiation to determine the native degradation of MB to understand the catalytic mechanism. The absorbance spectra of the organic pollutant were obtained using a UV-vis spectrophotometer (Varian Cary 100). The degradation of the MB dye molecules was monitored by measuring their real time absorption at 661 nm, and the relative concentrations of the pollutants ($C/C_0$) could demonstrate the photocatalytic activities with respect to time using a UV-vis spectrophotometer. The catalytic activity of commercially available Degussa P25 was compared with that of the 1D heterostructural NFs under different photoirradiation. The degradation efficiency of the dye solution was calculated using $((C_0 - C)/C_0) \times 100$, where $C$ and $C_0$ indicate the absorption peak intensities before and after the UV and visible irradiation. Additionally, the photocatalytic properties for colorless organic wastes (4-chlorophenol; 4-CP (10 ppm)) were investigated. In order to rule out the photosensitive effect, a colorless organic pollutant (4-CP) was used as the probe molecule to investigate the visible catalytic performance of the heterostructural catalytic NFs. In order to investigate the long term stability, the reusability of the sample was tested for twenty consecutive cycles under visible irradiation. Following every cycle, the old solution was removed and a fresh dye solution was added and induced under visible

irradiation. The stability of the catalysts were also investigated *via* SEM and X-ray diffraction studies after the reuse cycles.

### Active species trapping and superoxide radical quantification experiments

In order to gain insight into the mechanism between the catalytic heterostructures, the production and quenching rates of the reactive oxygen species (ROS) were investigated in a similar way to in the former photocatalytic activity test. NBT (100 mM, exhibiting an absorption maximum at 259 nm) and *p*-CBA (100 mM, exhibiting an absorption maximum at 232 nm) were used as the indicators to determine the amount of $O_2^{\bullet-}$ and $^{\bullet}OH$ generated in the heterostructural nanocatalyst[13,21] and a brief procedure is given in the supplementary information. For identifying the active species during the photocatalytic reaction, hydroxyl radicals ($^{\bullet}OH$), superoxide radicals ($O_2^{\bullet-}$), photogenerated electrons ($e^-$) and holes ($h^+$) were investigated by adding 1.0 mM IPA (a quencher of $^{\bullet}OH$), BQ (a quencher of $O_2^{\bullet-}$), $AgNO_3$ (a quencher of $e^-$) and TEOA (a quencher of $h^+$), respectively.[21–24] The method was similar to that of the former photocatalytic activity test.

## Result and discussion

Scheme 1 shows the different phases of the electrospun NFs going from composite to ternary structure as a function of the annealing temperature. To control the solid core NF morphology with preferred crystalline quality, the annealing temperature was varied from 500 °C to 800 °C and the samples were named ZnO–$TiO_2$ NF and $ZnTiO_3$ NF, which were later investigated with regards to their structural nature using XRD. The synthesized NF catalysts with the function of the annealing temperature were analyzed with regards to their visible catalytic response, and the comparative investigation between the composite and the ternary features was resolved.

Fig. 1 shows the X-ray diffraction spectra of the composite and ternary structural phases of the nanostructures. The XRD spectra of the samples annealed under 500 °C show the composite nature of the ZnO- and $TiO_2$-based crystalline planes, which clearly match with JCPDS card no: 89-1397 and 21-1272, representing the hexagonal phase of ZnO and the anatase phase of $TiO_2$, respectively. On increasing the annealing temperature to 800 °C, the structural phase clearly denotes the hexagonal phase of $ZnTiO_3$ (JCPDS card no: 26-1500) with mild traces of the cubic phase of $ZnTiO_3$. From observations, the transformation that occurs on increasing the annealing temperature to 800 °C denotes the lattice compression of $ZnTiO_3$ at the surface as a function of temperature. The function of the annealing temperature causes the transformation of the composite nature to the ternary phase with the furnished NF morphology (Fig. S1†). To analyze the pure forms of the different heterostructural interfaces, 500 °C and 800 °C annealed samples were chosen for the investigation and in between these annealing conditions the nanostructures exhibited the mixed phases of $ZnTiO_3$ and $TiO_2$ (600–700 °C), which have the sub-band defect levels though the oxygen vacancies and carbon doping possibilities.

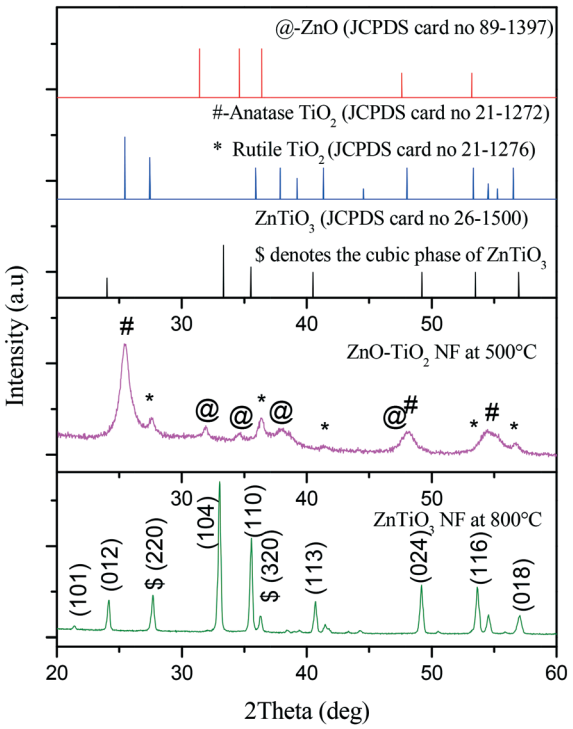


**Fig. 1** X-ray diffraction patterns of the ZnO–$TiO_2$ (annealed at 500 °C) and ternary $ZnTiO_3$ (annealed at 800 °C) samples with the comparative ZnO, $TiO_2$ and $ZnTiO_3$ standard patterns.

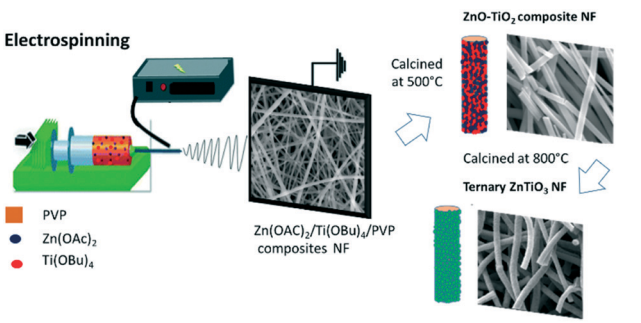


**Scheme 1** Synthesis process of the different structural phases of the heterostructural NFs as a function of the calcination temperature.

Fig. 2 shows the SEM images of the electrospun NFs as a function of different annealing temperatures. The morphological nature and the surface features reveal that the as prepared electrospun $Zn(OAc)_2$–$Ti(OBu)_4$-PVP NFs had a bead-free and smooth fibrous nature with a uniform diameter of 625 ± 85 nm (Fig. 2a and b). On annealing the electrospun NFs under 500 °C, the polymeric fibrous web transformed into the ZnO–$TiO_2$ composite with NF morphology with a reduction in the fiber diameter due to the degradation of the organic part (the PVP polymer matrix, acetate and butyl group) (Fig. 2c). As shown in Fig. 2d, the NF surface was smoother with a diameter of 425 ± 85 nm. On further increasing the annealing temperature to 800 °C, the surface of the

 

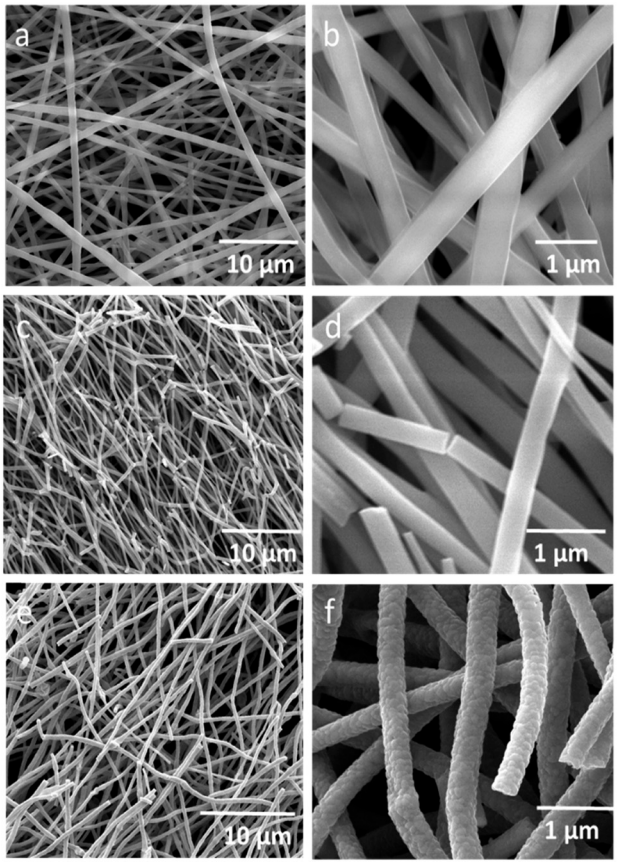


**Fig. 2** SEM images of (a and b) the as-electrospun $Zn(OAc)_2$–$Ti(OBu)_4$-PVP NF, (c and d) the ZnO–$TiO_2$ composite NFs (annealed at 500 °C), and (e and f) the ternary $ZnTiO_3$ NFs (annealed at 800 °C).

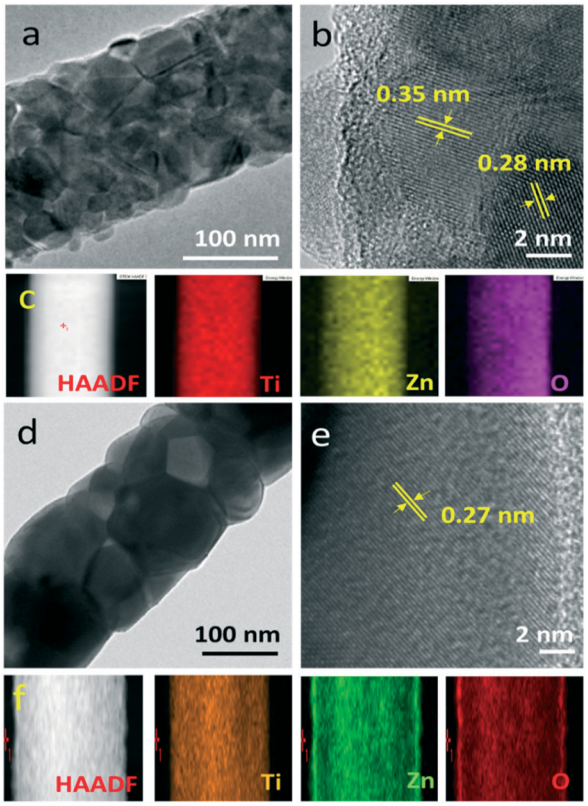


**Fig. 3** TEM and HRTEM of the annealing influence on the 1D NF (a and b) ZnO–$TiO_2$ composite NFs and (d and e) ternary $ZnTiO_3$ NFs, respectively. The EDAX-TEM elemental mapping images show the presence of elements (Zn, Ti, O) on the 1D fiber morphology of the (c) ZnO–$TiO_2$ composite NFs and (f) ternary $ZnTiO_3$ NFs.

NFs transformed into a grain assembled finish without any notable change to the diameter (Fig. 2e and f). The change in the surface morphology as a function of temperature reveals the influence of temperature on transforming the ZnO–$TiO_2$ composites into the ternary $ZnTiO_3$ phase NFs without any nanocluster forms of impurities. From the SEM images, we were not able to predict whether it was the ternary or composite form of the heterostructure and so TEM and HRTEM investigations were carried out further. The TEM analysis reveals the nanograin assembly with NF morphology in both sets of samples as a function of the annealing temperature (Fig. 3). In the grain assembly, we cannot visualise the composite or ternary functionality, but there is a clear contrast variation for distinguishing the lattice spacing for the different metal oxide nanograins. On annealing the NFs at 500 °C, the nanograins were closely packed with an average size of around 5–10 nm. On further increasing the annealing temperature to 800 °C, the nanograins diffused and formed closely packed large grains with an average size of 25 nm. The HRTEM results revealed the surface and crystalline nature of the nanograins with respect to the lattice spacing. Fig. 3b shows the HRTEM images of the ZnO–$TiO_2$ composite NFs at the surface that have two different lattice fringes with spacings of 0.350 nm and 0.274 nm, which represent the (101) plane of the anatase $TiO_2$ and the (100) plane of the hexagonal ZnO, which correlated well with the XRD results.[25,26]

However, the HRTEM images of the NFs that were annealed at 800 °C revealed the uniform distribution of fringes with a lattice spacing of 0.270 nm, which clearly represents the ternary form of $ZnTiO_3$ at the surface (Fig. 3e).[27] TEM and HRTEM studies cannot clearly show the elemental distribution in the composite and the ternary features of the NF morphology. The EDAX results reveal the presence of Zn, Ti and O on the NF surface (Fig. S2†). Elemental mapping studies were analyzed to understand the elemental composition and the extent of element distribution in the NF morphology. From the mapping studies (Fig. 3c), it was observed that the ZnO–$TiO_2$ composite forms NF morphology in the 500 °C annealed samples with the coexistence of Ti, Zn and O with uniform distribution. Further, the trace exhibition of C on the ZnO–$TiO_2$ NF surface was observed in Fig. S3.† Fig. 3f reveals that the mapping results of the 800 °C NFs were similar to those of the 500 °C annealed samples with the coexistence of Ti, Zn and O ions. The mapping clearly shows the ternary form of the Zn–Ti compositional assembly with an exhibition of Zn ion richness at the surface along with the Ti and O ions. Mapping reveals that a Ti richness

was observed at the core region, and the shell surface was Zn ion rich for the ternary phase. The mapping results convey that at a lower temperature of annealing, the uniform distribution of Zn and Ti in the form of the composite nature is found. On increasing the annealing temperature to 800 °C, the surface of the composite NFs changed to the ternary phase with the possible interaction of Zn with Ti mostly on the NF surface, which formed the $ZnTiO_3$-based shell layer. At higher temperatures, Zn interacts with Ti at the surface and promotes the $TiO_2$-based core, which results in the formation of the $TiO_2$–$ZnTiO_3$ form of the core–shell NFs. The temperature may induce the possibility of mobilizing the Zn ions to the surface to form the ternary phase at the surface as a shell layer.

The difference in the surface structural nature from the composite to the ternary feature causes a huge difference in the optical response, which was evidenced in the UV-vis DRS studies (Fig. 4a). In the bulk nature, as there are individual $TiO_2$ NFs and ZnO NFs, band gaps of 3.2 and 3.3 eV were exhibited, respectively,[1,28] and if they were in the ternary phase the band gap would be 3.6 eV, which has promising absorption only in UV irradiation.[29,30] But here, the synthesized composite form of the ZnO–$TiO_2$ NFs had broad absorption towards the visible region with the two sets of band edge absorptions and the possibility of few defect states *via* the carbon impurities and oxygen defect states. This is interesting for improving the visible response of the catalyst. Furthermore, this set of features is absent in the $ZnTiO_3$ NFs, which have a promising sharp band edge absorption of 425 nm, which represents the band absorption onset at 3.01 eV. This could be due to the elucidation of the band confinement by the heterostructural interface, which allows for the narrowing of the band function through the confinement of carrier separation in different ends, and which delays the carrier recombination. The band gaps of the NFs were calculated through the Kubelka–Munk (K-M) plot, which showed band gap energies of 2.10 eV and 3.01 eV for the ZnO–$TiO_2$ NFs and $ZnTiO_3$ NFs, respectively. It facilitates the abundant light response towards the visible region for favorable visible catalytic properties.

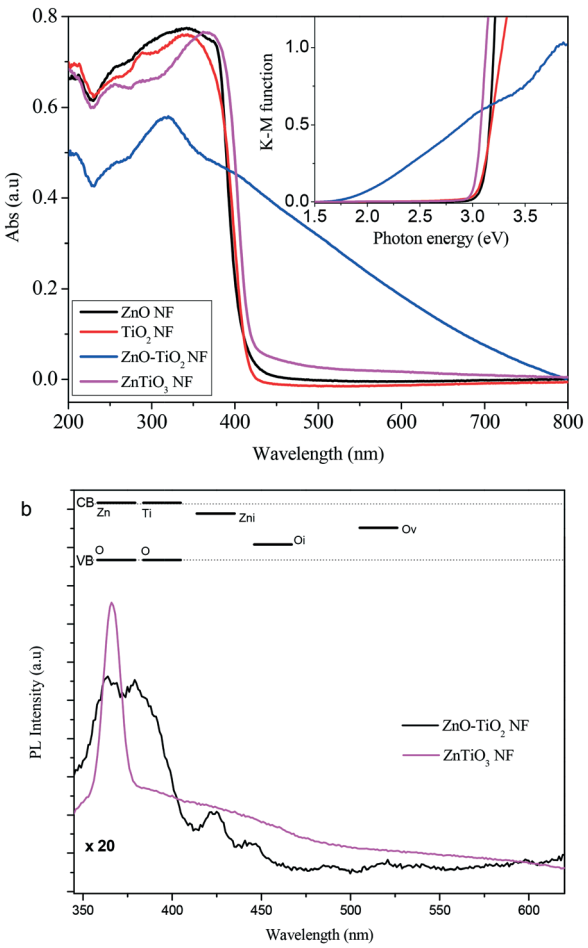


**Fig. 4** (a) UV-vis diffuse reflectance spectra and (b) photoluminescence of the ZnO, $TiO_2$, ZnO–$TiO_2$ composite and ternary $ZnTiO_3$ NFs. Inset shows the K-M function of the respective NFs.

Fig. 4b shows the photoluminescence spectra of the ZnO–$TiO_2$ composite and the $ZnTiO_3$ NFs under an excitation wavelength of 325 nm. The composite NFs have broad double split peaks between 350–400 nm, which represent the coupled band edge emission of the ZnO and $TiO_2$ nanograins. Meanwhile, the $ZnTiO_3$ NFs show a sharp emission peak around 362 nm for the the band edge emission of the ternary structure. The weak broad signal detected between 450–600 nm denotes the shallow and deep trap states due to the surface defect states.[28] As compared with the $ZnTiO_3$ NFs, the ZnO–$TiO_2$ composite natured NF samples exhibited the interstitial states of Zn ions and mild traces of oxygen vacancies in bluish and greenish emission states. Furthermore, ZnO–$TiO_2$ NFs have a very slow rate of carrier recombination when compared with the $ZnTiO_3$ NFs, which has been observed from the peak emission intensity when using the same quantity of the NF samples. However, from the observations, in both cases the NFs had the possibility of defect states, which played an effective role in the carrier extraction through the presence of localized surface states within the band gap. From analyzing the BET measurements on the heterostructural NFs, the ZnO–$TiO_2$ composites and ternary $ZnTiO_3$ NFs exhibited a surface area of 14.3 $m^2\ g^{-1}$ and 16.0 $m^2\ g^{-1}$, respectively, which were nearly similar (Fig. S4†). To further understand the chemical nature of the surface, an XPS investigation was conducted for the NF catalyst (Fig. 5).

Fig. 5a reveals the survey spectrum of the composite and ternary form of the catalytic surface and clearly exhibits the presence of O 1s, Ti2p, Zn2p, and C 1s core levels. Fig. 5b shows the high resolution Zn 2p spectra of the composite and ternary NFs with a comparison with pure ZnO NFs. The intense shaped peaks at 1022.01 eV and 1044.89 eV represent Zn $2p_{3/2}$ and Zn $2p_{1/2}$, respectively, with an energy difference of 22.9 eV, which is evidence of the exhibition of the $Zn^{2+}$ nature on the catalyst surface.[21,31] The mild shift in the Zn $2p_{3/2}$ denotes the strong Zn–O interaction with the Ti ions with the function of increasing the annealing temperature. Fig. 5c shows the high resolution Ti 2p scan profile that

 

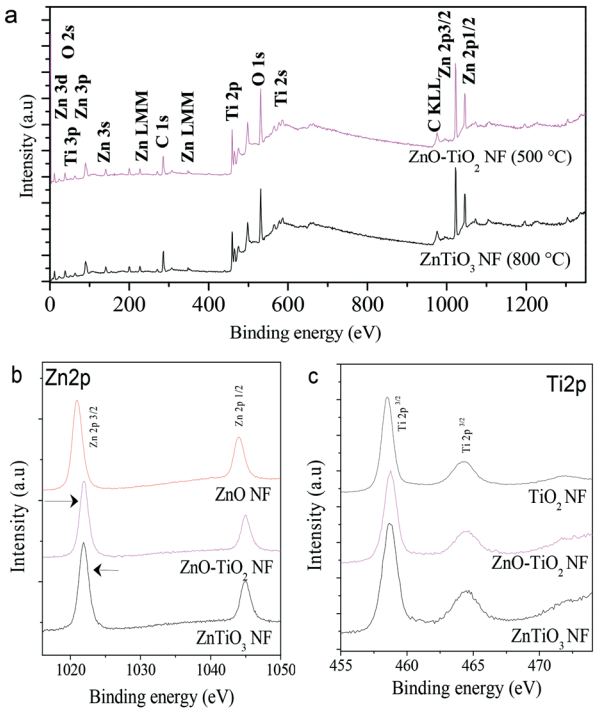


**Fig. 5** XPS spectra of the ZnO–$TiO_2$ composite NFs and ternary $ZnTiO_3$ NFs: (a) survey, (b) Zn 2p and (c) Ti 2p. The signals of the electrospun ZnO NFs and $TiO_2$ NFs were taken for a comparative investigation.

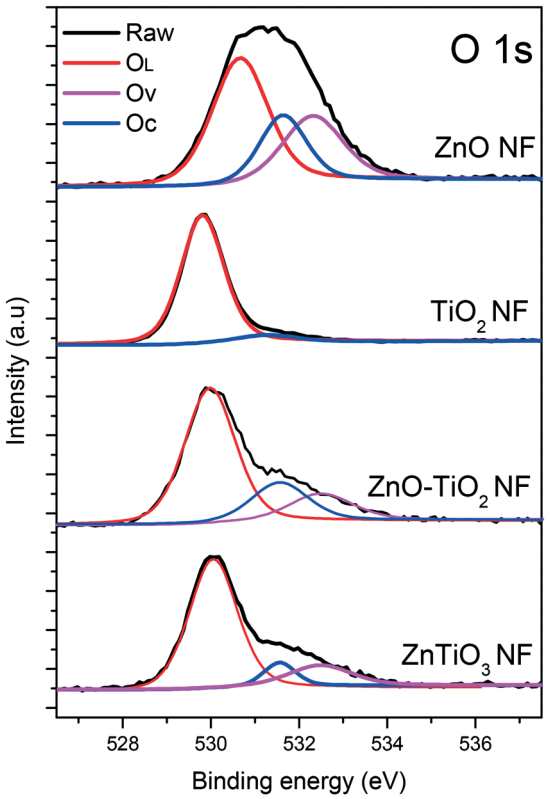


**Fig. 6** High resolution O 1s XPS spectra of (a) ZnO NFs, (b) $TiO_2$ NFs, (c) the ZnO–$TiO_2$ composite NFs (500 °C) and (d) the ternary $ZnTiO_3$ NFs (800 °C).

exhibits two broad peaks at 458.7 and 464.4 eV, which correspond to Ti $2p^{3/2}$ and Ti $2p^{1/2}$, respectively. On comparing with the spectrum peak of $TiO_2$ NF, the shift induced in the Ti $2p^{3/2}$ spectrum represents the possible interaction with the Zn ions at the surface in the form of Zn–O–Ti. The spectral separation between Ti $2p^{3/2}$ and Ti $2p^{1/2}$ is 5.7 eV, which represents the $Ti^{4+}$ nature on the catalytic surface.[29] The distinct atomic ratio difference between Zn : Ti (1.2 : 1) evidences the presence of a higher density of Zn at the catalyst surface for the higher annealing temperature form of the heterostructure. The increase in the Zn ratio at the catalytic surface as a function of the annealing temperature reveals the increase in the effective density of Zn ions in the form of $ZnTiO_3$ as a shell layer.

Fig. 6 shows the higher resolution scanning of the O 1s spectra of the composite NFs and ternary NFs with the comparative profiles of ZnO and $TiO_2$ NFs. On splitting the O 1s spectra with the Gaussian function, three spectral peaks were classified, representing lattice oxygen ($O_L$), nonlattice oxygen (oxygen vacancies) ($O_V$), and chemisorbed oxygen ions ($O_C$).[21] It can be clearly seen that the $O_L$ centered at 530.2 eV became intense and the $O_V$ reduced in the ternary sample due to the strong interaction of an O ion with the metal ions at the high temperature. The variation in the $O_V$ density represents the defect levels, and the relative percentages of the $O_L$ and $O_V$ states for all of the samples are noted in Table S1.† The presence of $O_C$ in the composite samples represents the possible interaction of a C ion with the O ions in the catalyst surface due to the unremoved carbon impurities arising due to the decomposition of the polymeric groups.[32] The trace exhibition of $O_V$ and $O_C$ at the catalyst surface leads to the possible interaction of organic pollutants at the catalyst surface, which leads to effective catalytic performance. Fig. S2† shows the C1s spectra of the composite NFs, evidencing the C–O interaction with the mild interaction of metal–C at 283.1 eV and showing the carbon doping in the catalyst surface.[33] However, it is absent in the ternary $ZnTiO_3$ feature, which reveals that the carbon phase impurities were removed at the higher temperature.

Fig. 7 shows the XPS valance band spectra of the ZnO–$TiO_2$ NFs and the $ZnTiO_3$ NFs. The $ZnTiO_3$ NF spectrum shows a VB maximum at 3.72 eV with a tail function extending to 2.86 eV, which represents the sub-band level created through the possibility of oxygen-based surface defect states. While coupling the calculated band gap from the UV DRS spectra (3.01 eV), the position of the CB minimum would occur at −0.15 eV. However, in the composite form, the VB maximum was exhibited at 2.98 eV with a strong tail in the band function up to 1.85 eV, which may be due to the strong doping of C ions, as well as the carbon impurity phases on the NF surface. By correlating the calculated bandgap with the VB position, the CB minimum was suggested to be −0.25 eV for the composite NFs. However, the exhibition of the strong two band function in the UV DRS

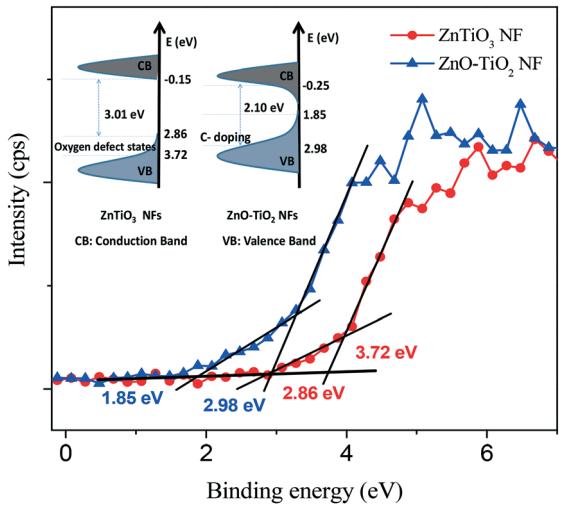


Fig. 7 Valence-band XPS spectra of the ZnO–$TiO_2$ NFs and $ZnTiO_3$ NFs. Inset shows the schematic illustration of the DOS of defect induced ZnO–$TiO_2$ NFs and the $ZnTiO_3$ NFs band structure.

spectra causes a discrete CB minima due to the presence of Zn interstitial defects, which is confirmed by the PL spectra. The inset shows the schematic illustration of the density of states (DOS) of the ZnO–$TiO_2$ NFs and $ZnTiO_3$ NFs with the presence of the defect states. Furthermore, the role of the carbon impurities and Zn interstitial states on the ZnO–$TiO_2$ NF surface induces the narrow band gap by inducing the change in the VB and CB positions. The demonstrated possibility of the band energy shift in the VB and CB positions was seen in the XPS and UV visible DRS results.

The conformal evidential classification from two sets of nanostructures such as the composite and ternary catalysts was revealed from the XRD, HRTEM, EDS mapping and DRS studies. The visible photocatalytic properties of the ternary phase of the NF catalyst were tested under fatal organic pollutant dye (MB) water. Without any catalyst, the MB dye solution was nearly stable under visible irradiation with a self-degradation rate of 5% (Fig. S5†). Fig. 8 and S6† show that the photocatalytic properties of the $TiO_2$ and ZnO NFs were unfavorable, as they exhibited a degradation efficiency of 27.89% and 58.84%, respectively, under visible light irradiation in 125 min. The reasons for their visible activity were discussed in our previous investigations.[13,21] When using the composite and ternary forms of the heterostructural catalyst, the degradation activity was promoted under visible irradiation. The ternary $ZnTiO_3$ NFs displayed a visible catalytic degradation efficiency of 72.43% in 125 min. However, the $TiO_2$–ZnO composite NFs exhibited a pronounced degradation efficiency of 95.82% in 125 min for the MB dye solution under similar conditions. The calculation of the kinetics of the catalytic reaction were fit using the pseudo first order reaction model with a linear fit. The degradation rates ($k$) of the catalytic NFs under visible irradiation were calculated to be 0.0033 $min^{-1}$, 0.0091 $min^{-1}$, 0.0212 $min^{-1}$ and 0.0121 $min^{-1}$ for the ZnO, $TiO_2$, $TiO_2$–ZnO composite and ternary $ZnTiO_3$

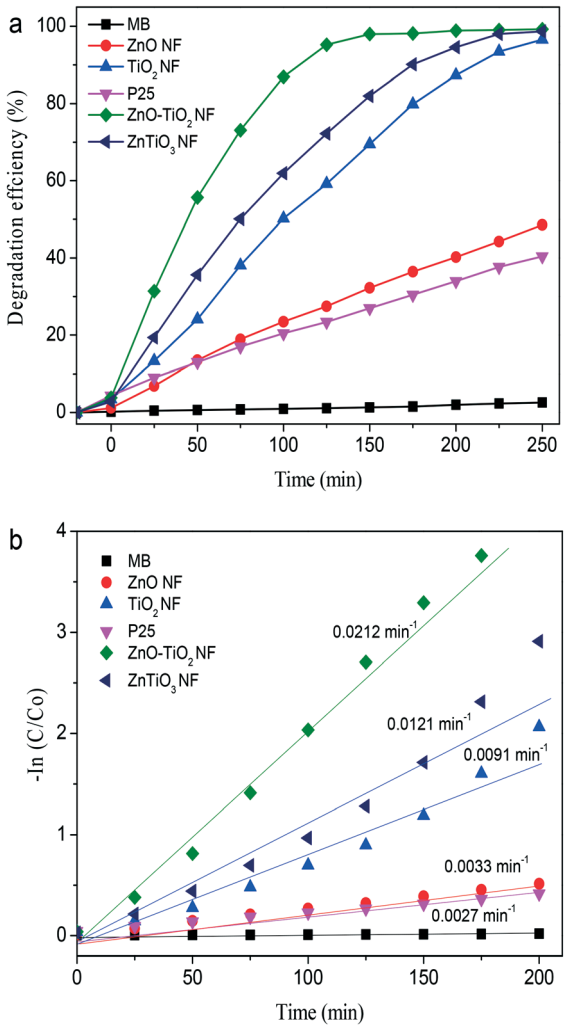


Fig. 8 Photodegradation performance (a) and the degradation rate (b) of MB under visible irradiation ($\lambda > 400$ nm) for the electrospun ZnO, $TiO_2$, ZnO–$TiO_2$ and $ZnTiO_3$ NFs and for P25.

catalytic NFs. The photoresponsive behavior of the NF catalyst is tabulated in Table 1 to understand the photoresponsive nature in a different set of crystalline phases. The commendable visible catalytic response in the $TiO_2$–ZnO form of the composite NFs as compared with its single counterparts ($TiO_2$ NFs and ZnO NFs) showed the benefit of improved carrier mobility through the band structures with a tunable visible light harvesting response with the favor of defect states.

The constructed ternary $ZnTiO_3$ form of the NF assembly is credited with improving the carrier separation rate, and the light harvesting nature in the visible region was restricted beyond 425 nm because of the proper set of band functions without any defect impurities. The extensive factors in the band function that originate a visible catalytic response are the defect states, which improve the interfacial contact between the $TiO_2$ and ZnO and promote the separation of photogenerated electrons and hole carriers in the form of the composite assembly. The grain interfaces in the composite

 

**Table 1** Photoresponsive nature, calculated bandgap, CB position and VB position of the ZnO, $TiO_2$, ZnO–$TiO_2$ composite and ternary $ZnTiO_3$ NFs

| Sample | Band gap | Dye adsorption efficiency under dark conditions in 125 min | Catalytic efficiency under UV irradiation in 125 min | Catalytic efficiency under visible irradiation in 125 min | Catalytic rate under visible irradiation | CB position | VB position |
|---|---|---|---|---|---|---|---|
| ZnO NFs | 3.21 eV | 4.23% | 79.11% | 27.89% | 0.0033 $min^{-1}$ | −0.31 eV | 2.90 eV |
| $TiO_2$ NFs | 3.17 eV | 10.83% | 89.19% | 58.84% | 0.0091 $min^{-1}$ | −0.29 eV | 2.88 eV |
| ZnO–$TiO_2$ NFs | 2.10 eV | 15.27% | 98.76% | 95.82% | 0.0212 $min^{-1}$ | −0.25 eV | 1.85–2.98 eV |
| $ZnTiO_3$ NFs | 3.01 eV | 17.39% | 98.35% | 72.43% | 0.0121 $min^{-1}$ | −0.07 eV | 2.86–3.78 eV |
| P25 | 3.32 eV | 14.64% | 70.34% | 23.64% | 0.0027 $min^{-1}$ | — | — |

nature of ZnO–$TiO_2$ induce a type II band function, which improves the freedom to enhance the carrier separation rate. It evidences more advantages than the $ZnTiO_3$ structure with a longer wavelength response and a narrow band function. The composite form of the NFs induces type II band structures with closely packed grain interfaces associated with the defect levels, with an impact on the commendable visible catalytic response. The existence of the composite functionality at the surface with the defect state functionality improves the collection and transportation of the carriers when compared to the ternary phase of $ZnTiO_3$. To validate the difference in the band function, the band offsets in the composite and ternary structures were investigated through calculating the band gap positioning of the conduction and valance band of the catalyst functionality. The band position of the catalysts was calculated and tabulated (Table 1). For the composite form, we were able to clearly visualise the clear band function, and thus the single counterparts were considered for determining the band function. The conduction band (CB) and valence band (VB) values were calculated using the band gaps of $TiO_2$, ZnO and $ZnTiO_3$ obtained from the UV-DRS spectra band gaps of the catalytic NFs. The band diagrams of the catalytic NFs are presented in Fig. 9 and reveal the carrier mobility under visible irradiation with a type II band alignment, depending on their band positions. In the ternary $ZnTiO_3$ form, through the mild visible responsive band function (3.01 eV), photogenerated electrons move from the CB of $ZnTiO_3$ and favour the production of super oxide radicals under photoirradiation.

On the other hand, the ZnO–$TiO_2$ composite NFs with heterostructural grain interfaces (Fig. 9) and carbon based impurities lead to effective visible responses with an improved carrier separation rate. Thus the electrons move to the CB of the $TiO_2$ and the holes move towards the VB of ZnO through carbon doping and surface defect levels with an effective carrier separation rate. There is an identical type II band structure in the composite featured catalytic surface with multiple grain interfaces, but the ternary interface induces only a mild trace of the carrier separation properties through the limited visible responsive nature through the possibility of defect states. In the form of the nanograined composites, ZnO and $TiO_2$ nanograins are closely packed at

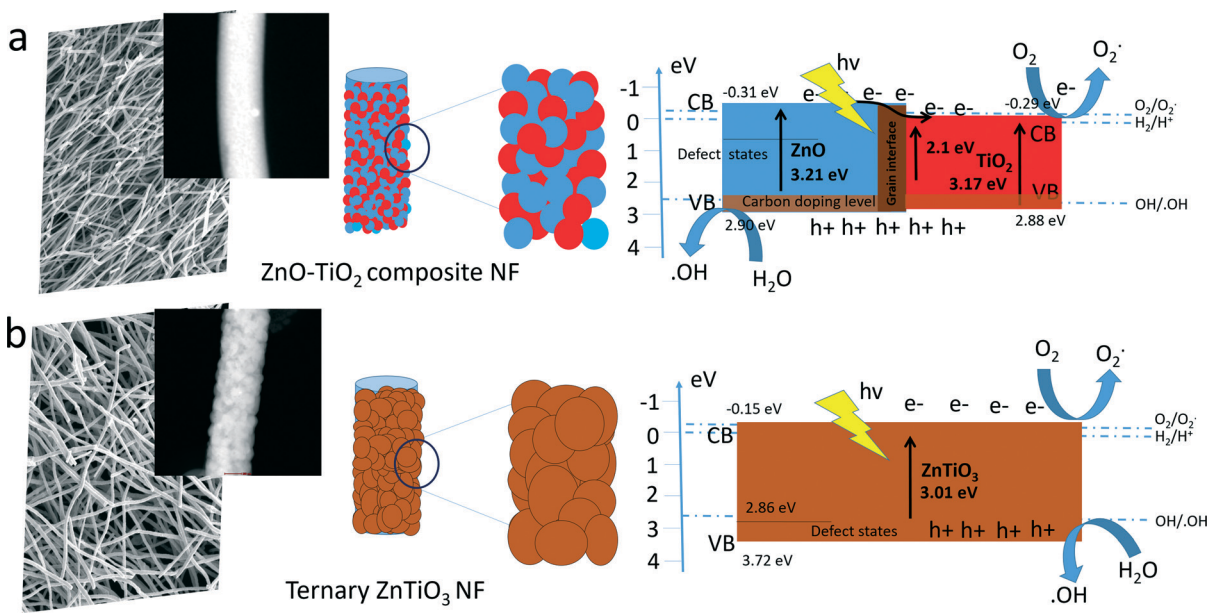


**Fig. 9** Schematic band diagram and charge transfer mechanism in the NF surface catalyst under visible light illumination for (a) the ZnO–$TiO_2$ composite NFs and (b) the ternary $ZnTiO_3$ NFs.

the surface with an improved carrier transfer rate to the surface, which leads to the superior catalytic performance through the retardation of the carrier recombination rate as compared with the solid $ZnTiO_3$ shell finish.

Both sets of catalysts were found to be effective catalysts under visible irradiation because of the visible light absorptive nature of the heterostructures. As compared with the ternary $ZnTiO_3$ form of the NFs, the $TiO_2$–ZnO-based composite NFs embolden the visible catalytic performance through their enhanced light harvesting ability for the accountability of superior visible catalytic performance through the possibility of carbon impurities and surface defect states. To preclude the effect of the photosensitivity of the dye molecules under visible irradiation, the visible catalytic performance of the heterostructural NF-based catalysts were investigated towards the degradation of colorless 4-cholorophenol, and the results are shown in Fig. S6.† As expected, the ZnO–$TiO_2$ composites had an impressive degradation nature of around 67.21% as compared with the ternary architecture (46.56%) under 120 min of visible irradiation. On investigating the photocatalytic responses of the composite and ternary NFs under UV irradiation, they were found to be similar to those from the visible result and the composite NFs exhibited the higher catalytic efficiency. However, the degradation rate difference has slightly improved for the ternary NFs under UV irradiation as compared with their visible catalytic performance (Fig. S7†) because of the promising UV responsive behavior of the $ZnTiO_3$ NFs. Both sets of degradation results reveal that the catalysts are active with a similar degradation rate difference to the different dye solutions. To understand the mechanism behind the visible catalytic performances of the heterostructural NF catalyst, the engaging of the production rate of the ROS such as $O_2^{\bullet-}$ and $^{\bullet}OH$ has to quantify the mechanism of the advanced oxidation process in the photodegradation reactions. The catalytic activity of the ZnO promisingly depends on the production of the super oxides and the $TiO_2$ has the promising production nature of hydroxyl radicals under photoirradiation.[34] Both of these catalysts have the ability to produce all three radical species ($O_2^{\bullet-}$, $^{\bullet}OH$ and $^1O_2$) through the nature of their band potentials.[34] Therefore, coupling both catalytic nanostructures in one phase favors the production rate of the ROS for an effective catalytic response. To quantify the $O_2^{\bullet-}$ and $^{\bullet}OH$ production rate, NBT and *p*-CBA were used as probe molecules under visible irradiation (Fig. S8†).

Both sets of catalytic NF assemblies evidenced the production of $O_2^{\bullet-}$ and the $^{\bullet}OH$ radical, but the ZnO–$TiO_2$ composite NFs exhibited the higher production rate of $O_2^{\bullet-}$ and the $^{\bullet}OH$ radical, which was nearly twice higher than the production rate of the ternary NFs (Fig. 10). For further evidence, serious trapping investigations were done to quantify the active species engaged in the catalytic reactions. Different trapping elements such as $AgNO_3$ (to trap conduction band electrons), TEOA (to trap valance band holes), BQ (to trap superoxide radicals) and IPA (to trap hydroxyl radicals) were introduced to quantify the radical production rate from the hetero-

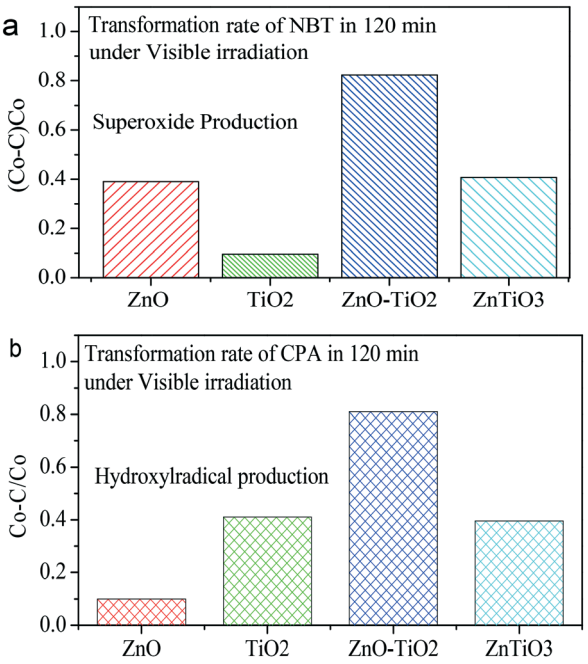


**Fig. 10** ROS quantification for the ZnO, $TiO_2$, ZnO–$TiO_2$ and $ZnTiO_3$ NFs from the transformation rate of the NBT (a) and *p*-CBA (b) concentration in 125 min for quantifying superoxide species and hydroxyl radicals under visible irradiation.

structural catalytic surface.[35] As observed from the results shown in Fig. 11, on introducing IPA (hydroxyl radicals trappers), BQ (superoxide trappers), TEOA (photogenerated holes) and $AgNO_3$ (photogenerated electrons) there was an effective reduction in the photocatalytic performance in the ZnO–$TiO_2$ composite NFs. However, the ternary NFs revealed a decline in the catalytic response only under the introduction of IPA (hydroxyl radicals trappers), BQ (superoxide trappers) and $AgNO_3$ (photogenerated electrons), and not much influence was seen on introducing TEOA (photogenerated holes). From these observations, the following mechanism has been used to propose a charge separation nature at the catalyst surface.

$$ZnTiO_3 + h\nu \rightarrow ZnTiO_3(e_{CB}^- \ldots h_{VB}^+) \quad (1)$$

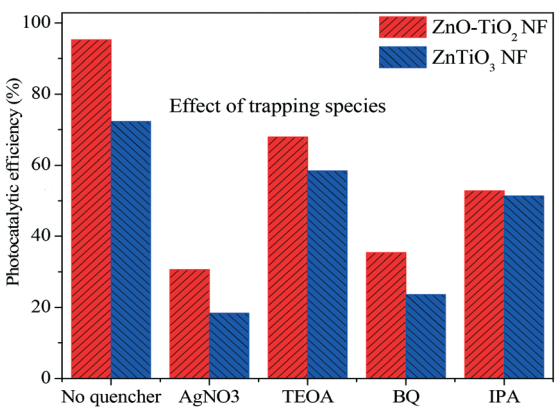


**Fig. 11** Trapping experiment of the active species during the photocatalytic reaction under 125 min of Xe lamp irradiation.

$$ZnTiO_3(e_{CB}^-) + O_2 \rightarrow ZnTiO_3 + O_2^{\bullet -} \quad (2)$$

$$ZnTiO_3(h_{VB}^+) + OH \rightarrow ZnTiO_3 + {}^{\bullet}OH \quad (3)$$

$$ZnO + TiO_2 + h\nu \rightarrow ZnO(e_{CB}^- \ldots h_{VB}^+) + TiO_2(e_{CB}^- \ldots h_{VB}^+) \quad (4)$$

$$TiO_2(e_{CB}^-) + ZnO \rightarrow TiO_2 + ZnO(e_{CB}^-) \quad (5)$$

$$ZnO(h_{VB}^+) + TiO_2 \rightarrow ZnO + TiO_2(h_{VB}^+) \quad (6)$$

$$ZnO(e_{CB}^-) + O_2 \rightarrow TiO_2 + O_2^{\bullet -} \quad (7)$$

$$TiO_2(h_{VB}^+) + OH \rightarrow TiO_2 + OH^{\bullet} \quad (8)$$

$$O_2^{\bullet -} + H_2O \rightarrow HO_2^{\bullet} + OH- \quad (9)$$

$$HO_2^{\bullet} + H_2O \rightarrow OH^{\bullet} + H_2O_2 \quad (10)$$

$$H_2O_2 \rightarrow 2OH^{\bullet} \quad (11)$$

$$OH^{\bullet} + MB \rightarrow H_2O + CO_2 + \text{Degraded product} \quad (12)$$

In the ternary $ZnTiO_3$ structure, $ZnTiO_3$ is a mildly visible active photosensitizer ($\lambda$ = 412 nm), which transfers the excited electrons to the CB. Thus, the photogenerated electrons interact with the molecular oxygen and produce $O_2^{\bullet -}$ radicals and the photogenerated holes interact with the water molecules and produce hydroxyl radicals.[36] Furthermore, through consecutive reactions the superoxide radicals result in the formation of $^{\bullet}OH$ radicals, which favor the degradation of dye molecules. The effective adsorptive nature of the catalytic surface favours the dye molecules interacting with the radical species at the surface and increases the rate of the catalytic reaction. The mild visible response on $ZnTiO_3$ NFs reveals the slower production rate of the radical species on the catalytic surface under visible irradiation. However, in the ZnO–$TiO_2$-based composite NFs, the defect induced levels revealed the narrow band function, which promoted the ZnO and $TiO_2$ as visible sensitizers. Because of the type-II band function with the negative band potential, photogenerated electrons and holes were separated between ZnO and $TiO_2$, which caused a delay in the carrier recombination. Photogenerated electrons and holes in the ZnO and $TiO_2$ were represented by the production rate of $O_2^{\bullet -}$ and $^{\bullet}OH$ radicals on the catalytic surface, and both CB electrons and VB holes were engaged in the production of the ROS for the effective photocatalytic process. From these observations, the photogenerated electrons are the most engaging and ruling active species in both the composite and ternary phase catalysts and assist in the production of $O_2^{\bullet -}$ and $^{\bullet}OH$.

The nanograined composite phase reveals a lower recombination rate with an effective carrier separation efficiency under visible irradiation through the defect induced trap states. After attaining the effective visible catalytic response of the catalytic surface, reusability and stability are the rising concerns to exhibit in a promising catalyst. We have investigated the catalytic performance for 20 consecutive degradation cycles of MB with the ZnO–$TiO_2$ composites and ternary $ZnTiO_3$ NFs (Fig. 12). After multiple consecutive cycles, the ZnO–$TiO_2$ composite NFs lost nearly 34.21% of their catalytic performance and the $ZnTiO_3$ NFs eventually lost 12.54% of their degradation efficiency under visible irradiation on comparison with their 1st cycle performance. There is a possibility of unpreventable catalyst loss during the reuse process, but it was minimised throughout the reuse process because of the web form of the NF assembly (Fig. S9†). The morphological investigation performed after multiple reuse cycles reveals that the composite NFs lost their surface structural morphology but the $ZnTiO_3$ NFs were quite stable after the multiple reuse cycles (Fig. 12b and c). This may be due to the effective photocorrosive nature of the Zn ions or to leaching of the metal ions during the catalytic process, but the $ZnTiO_3$ shell layer was quite more stable under the reuse process, evidencing the photocorrosive stability of the surface feature. The XRD spectra of the catalyst after multiple recycles show that there was no notable change in the structural nature of the catalyst before and after the degradation process (Fig. S10†). Control over the structural surface investigation induces the development of the visible catalytic functionality on the heterostructural interfaces through improved light responses coupled with a suppressive carrier recombination rate. Changing the structural nature of similar compositions with unchanged NF morphology has created interest in understanding the carrier mobility to improve catalytic performance. The obtained results forecast the potential advantages of the structural merits for the development of visible

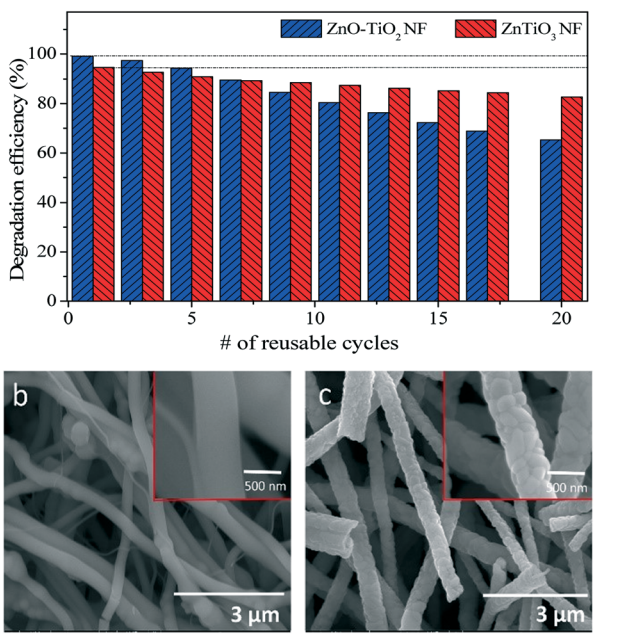


Fig. 12 (a) Degradation efficiency of the ZnO–$TiO_2$ composite and ternary $ZnTiO_3$ NFs with an increasing number of catalytic cycles. (b and c) SEM images of the ZnO–$TiO_2$ composite and ternary $ZnTiO_3$ NFs after 20 photocatalytic runs.

responsive natures with durable and reusable 1D nanofibrous catalysts.

## Conclusion

Our investigation reveals the advantages of the surface structural functionality of 1D NFs with the function of annealing temperature toward the exhibition of visible photocatalytic performances. The surface structural defect states lead to a tunable visible light adsorptive nature with an effective carrier separation rate that promotes the visible catalytic performance. In the heterostructural form, the ZnO–$TiO_2$ composite NFs exhibited a more commendable visible catalytic efficiency than that of the $ZnTiO_3$ NFs, which was credited to their structural defects and carbon impurities that maximized the carrier separation and transportation rate with a favorable narrow band function through carbon doping functionality. The trapping experiment results showed the light responsive mechanism of the different band structures of the heterostructural NFs. The possible favorable production rate of superoxides ($O_2^{\bullet-}$) shows that they are the ruling active species for the degradation of dye molecules under visible irradiation. The tunable surface structural features lead to the durable and reusable sustainability of the electrospun NFs during the photocatalytic process, which allows for the exploration of them as a promising robust form of photocatalyst.

## Conflicts of interest

There are no conflicts to declare.

## Acknowledgements

K. S. Ranjith acknowledges The Scientific & Technological Research Council of Turkey (TUBITAK), BIDEB 2216-Fellowships for Research Fellowship Programme for Foreign Citizens for his postdoctoral fellowship.

## References

1 S. Hernandez, D. Hidalgo, A. Sacco and A. Chiodon, *Phys. Chem. Chem. Phys.*, 2015, **17**, 7775–7786.
2 R. P. Souza, E. Ambrosio, M. T. F. Souza, T. K. F. S. Freitas, A. M. Ferrari-Lima and J. C. Garcia, *Environ. Sci. Pollut. Res.*, 2017, **24**, 12691–12699.
3 J. Li and N. Wu, *Catal. Sci. Technol.*, 2015, **5**, 1360–1384.
4 P. Sudhagar, A. Devadoss, T. Song, P. Lakshmipathiraj, H. Han, V. V. Lysak, C. Terashima, K. Nakata, A. Fujishima, U. Paik and Y. S. Kang, *Phys. Chem. Chem. Phys.*, 2014, **16**, 17748–17755.
5 D. S. Ovoshchnikov, B. G. Donoeva and V. B. Golovko, *ACS Catal.*, 2015, **5**, 34–38.
6 R. Long, N. J. English and O. V. Prezhdo, *J. Am. Chem. Soc.*, 2013, **135**, 18892–18900.
7 F. M. Pesci, G. Wang, D. R. Klug, Y. Li and A. J. Cowan, *J. Phys. Chem. C*, 2013, **117**, 25837–25844.
8 J. Tian, Z. Zhao, A. Kumar, R. I. Boughtonc and H. Liu, *Chem. Soc. Rev.*, 2014, **43**, 6920–6937.
9 M. S. Vitiello, L. Viti, D. Coquillat, W. Knap, D. Ercolani and L. Sorba, *APL Mater.*, 2015, **3**, 026104.
10 Na. Wu, C. Wang, P. M. Slattum, Y. Zhang, X. Yang and L. Zang, *ACS Energy Lett.*, 2016, **1**, 906–912.
11 W. Feng, Y. Wang, X. Huang, K. Wang, F. Gao, Y. Zhao, B. Wang, L. Zhang and P. Liu, *Appl. Catal., A*, 2018, **220**, 324–336.
12 S. M. Myers, W. R. Wampler and N. A. Modine, *J. Appl. Phys.*, 2016, **120**, 134502.
13 K. S. Ranjith and T. Uyar, *J. Mater. Chem. A*, 2017, **5**, 14206–14219.
14 N. Guijarro, E. Guillen, T. L. Villarreal and R. Gomez, *Phys. Chem. Chem. Phys.*, 2014, **16**, 9115–9122.
15 M. Li, J. Wang, P. Zhang, Q. Deng, J. Zhang, K. Jiang, Z. Hu and J. Chu, *Sci. Rep.*, 2017, **6**, 42484.
16 F. Haque, T. Daeneke, K. Kalantar-zadeh and J. Z. Ou, *Nano-Micro Lett.*, 2018, **10**, 23.
17 P. Zhang, C. Shao, M. Zhang, Z. Guo, J. Mu, Z. Zhang, X. Zhang and Y. Liu, *J. Hazard. Mater.*, 2012, **217-218**, 422–428.
18 Y. Duan, L. Liang, K. Lv, Q. Li and M. Li, *Appl. Surf. Sci.*, 2018, **456**, 817–826.
19 J. Zhang, H. Lu, C. Liu, C. Chen and X. Xin, *RSC Adv.*, 2017, **7**, 40499–40509.
20 J. Cao, Z. Wang, R. Wang, S. Liu, T. Fei, L. Wang and T. Zhang, *RSC Adv.*, 2015, **5**, 36340–36346.
21 K. S. Ranjith, A. Senthamizhan, B. Balusamy and T. Uyar, *Catal. Sci. Technol.*, 2017, **7**, 1167–1180.
22 S. Ren, B. Wang, H. Zhang, P. Ding and Q. Wang, *ACS Appl. Mater. Interfaces*, 2015, **7**, 4066–4074.
23 Y. Su, H. Wang, L. Ye, X. Jin, H. Xie, C. He and K. Bao, *RSC Adv.*, 2014, **4**, 65056–65064.
24 Y. Chen, G. Tian, Q. Guo, R. Li, T. Hana and H. Fu, *CrystEngComm*, 2015, **17**, 8720–8727.
25 Y. Chimupala, G. Hyett, R. Simpson, R. Mitchell, R. Douthwaite, S. J. Milne and R. D. Brydson, *RSC Adv.*, 2014, **4**, 48507–48515.
26 S. Kumar, N. Tiwari, S. N. Jha, S. Chatterjee, D. Bhattacharyya, N. K. Sahoo and A. K. Ghosh, *RSC Adv.*, 2015, **5**, 94658–94669.
27 R. C. Pawar, S. Kang, J. H. Park, J. H. Kim, S. Ahn and C. S. Lee, *Catal. Sci. Technol.*, 2017, **7**, 2579–2590.
28 C. Cheng, A. Amini, C. Zhu, Z. Xu, H. Song and N. Wang, *Sci. Rep.*, 2014, **4**, 4181.
29 R. S. Raveendra, P. A. Prashanth, R. Hari Krishna, N. P. Bhagya, B. M. Nagabhushana, H. R. Naika, K. Lingaraju, H. Nagabhushana and B. Daruka Prasad, *J. Asian Ceram. Soc.*, 2014, **2**, 357–365.
30 A. Sachse, V. Hulea, K. L. Kostov, E. Belamie and B. Alonso, *Catal. Sci. Technol.*, 2015, **5**, 415–427.
31 D. Xu, D. Fan and W. Shen, *Nanoscale Res. Lett.*, 2013, **8**, 46.

 

32 T. Laurila, S. Sainio and M. A. Caro, Hybrid carbon based nanomaterials for electrochemical detection of biomolecules, *Prog. Mater. Sci.*, 2017, **88**, 499–594.
33 D. K. Mishra, J. Mohapatra, M. K. Sharma, R. Chattarjee, S. K. Singh, S. Varma, S. N. Behera, S. K. Nayak and P. Entel, *J. Magn. Magn. Mater.*, 2013, **329**, 146–152.
34 Y. Li, W. Zhang, J. Niu and Y. Chen, *ACS Nano*, 2012, **6**, 5164–5173.
35 Q. Yang, F. Chen, X. Li, D. Wang, Y. Zhong and G. Zeng, *RSC Adv.*, 2016, **6**, 60291–60307.
36 S. Girish Kumar and K. S. R. Koteswara Rao, *RSC Adv.*, 2015, **5**, 3306–3351.